

Two-dimensional magnetism in α -CuV₂O₆A. M. Golubev¹, J. Nuss¹, and R. K. Kremer^{1*}*Max Planck Institute for Solid State Research, 70569 Stuttgart, Germany*E. E. Gordon and M.-H. Whangbo²*Department of Chemistry, North Carolina State University, Raleigh, North Carolina 27695-8204, USA
and State Key Laboratory of Structural Chemistry, Fujian Institute of Research on the Structure of Matter (FJIRSM),
Chinese Academy of Sciences (CAS), Fuzhou 350002, People's Republic of China*

C. Ritter

*Institut Laue-Langevin, F-38042 Grenoble, France*L. Weber³ and S. Wessel*Institute for Theoretical Solid State Physics, RWTH Aachen University, 52074 Aachen, Germany* (Received 1 July 2019; revised 29 June 2020; accepted 30 June 2020; published 21 July 2020)

Several previous studies reported that a one-dimensional Heisenberg chain model is inadequate in describing the magnetic properties of the low-dimensional quantum antiferromagnet α -CuV₂O₆, but the origin for this observation has remained unclear. We have reinvestigated the magnetic properties of α -CuV₂O₆ and found that our anisotropic magnetic susceptibility, neutron-powder diffraction, and electron paramagnetic spin-resonance measurements are in good agreement with extensive density-functional theory (DFT + *U*) total energy calculations which indicate that the correct spin lattice model for α -CuV₂O₆ is rather a $S = 1/2$ 2D-Heisenberg antiferromagnetic lattice. The magnetic susceptibility data are well described by a rectangular Heisenberg antiferromagnet with anisotropy ratio $\alpha \sim 0.7$ consistent with the DFT results. Quantum Monte Carlo simulations of the magnetic susceptibilities for a rectangular lattice Heisenberg antiferromagnet were performed in the anisotropy range $0.5 \leq \alpha \leq 1.0$. The results of the Quantum Monte Carlo calculations were cast into a Padé approximant which was used to fit the temperature-dependent magnetic susceptibility data. Neutron-powder-diffraction measurements were used to conclusively solve the collinear antiferromagnetic structure of α -CuV₂O₆ below the Néel temperature of ~ 22.4 K.

DOI: [10.1103/PhysRevB.102.014436](https://doi.org/10.1103/PhysRevB.102.014436)**I. INTRODUCTION**

Interest in low-dimensional quantum magnetic systems is motivated by the observation that such systems are model candidates to test theoretical predictions for exotic ground states with unusual excitations that are conceptually different from the standard behavior of three-dimensional (3D) magnetic systems [1–4]. For example, one-dimensional (1D) arrangement of Cu²⁺ spin $S = 1/2$ ions in CuL₂ *ribbon chains* (where L are ligands such as O, Cl, or Br) have recently proved to exhibit unusual magnetic and magnetoelectric ground-state properties [5–15]. Such ribbon chains are made up of square-planar CuL₄ plaquettes sharing their opposite edges. The Cu–L–Cu bonding angle of the nearest-

neighbor (NN) spin-exchange paths are close to 90°, which makes the NN spin exchange weak and usually ferromagnetic (FM) [16–18], whereas the next-nearest neighbor (NNN) spin exchange (super-superexchange), via Cu–L . . . L–Cu paths, is antiferromagnetic (AFM) and generally stronger in magnitude than the NN spin exchange [5–8,10–12]. The spin frustration resulting from the competition between the NN FM and NNN AFM spin exchanges provides a prolific playground for novel fluidlike ground states with unconventional excitations and properties like type-II multiferroicity based on incommensurate cycloid-type magnetic structures or spin nematicity in external magnetic fields [19–26]. In the present paper, we re-examine the magnetic properties of the low-dimensional quantum antiferromagnet α -CuV₂O₆ which in earlier studies has been analyzed in terms of a 1D Heisenberg magnet with uniform NN AFM spin exchange [27–29]. From the structural point of view, α -CuV₂O₆ features such CuO₂ ribbon chains resulting from trans-edge-sharing CuO₆ octahedra, which are axially elongated due to a Jahn-Teller distortion (see Fig. 1). Lately, α -CuV₂O₆ has also attracted attention because of its catalytic and photocatalytic activity and as a possible

*rekre@fkf.mpg.de

Published by the American Physical Society under the terms of the [Creative Commons Attribution 4.0 International](https://creativecommons.org/licenses/by/4.0/) license. Further distribution of this work must maintain attribution to the author(s) and the published article's title, journal citation, and DOI. Open access publication funded by the Max Planck Society.

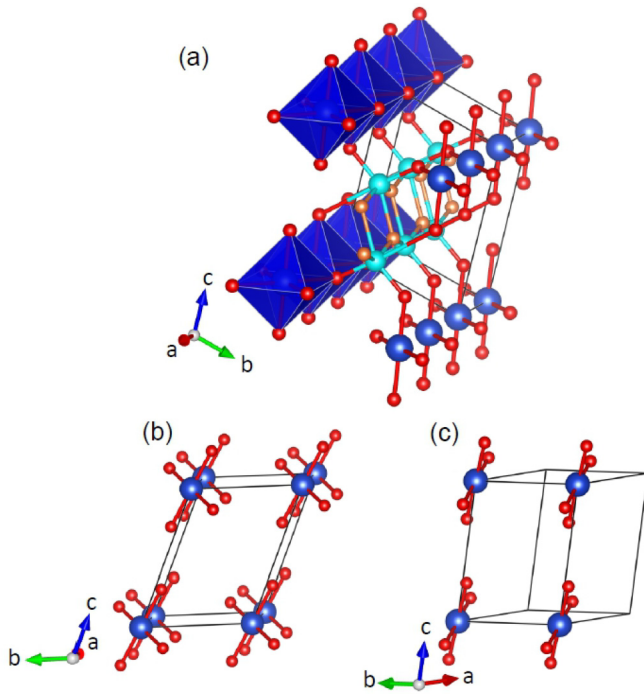


FIG. 1. (a) Crystal structure of α - CuV_2O_6 (in $P-1$ setting space group No. 2 [34]). The blue and cyan spheres show the Cu and V atoms, respectively. The small red spheres represent the oxygen atoms (O2, O3) in the distorted octahedral coordination around the Cu atoms. The orange spheres are oxygen atoms (O1) coordinating to V atoms exclusively. Note that we have chosen to present the triclinic crystal structure in $P-1$ setting of space group No. 2. In this setting, the shortest Cu–Cu distance is encountered along [100] whereas in $C-1$ setting used before in literature [27–29], the shortest Cu–Cu approach is found along the b direction. (a) Right: Arrangement of the CuO_4 stack-chains running along the a direction. (b), (c) Two NN CuO_4 planes along the b and c directions, defining the $J_{b,c}$ exchange paths.

active material for primary and rechargeable lithium batteries [30–33].

Essentially guided by the crystal structure, all preceding studies of the magnetic properties of α - CuV_2O_6 have assumed that the dominant spin exchange is the intrachain spin exchange along the a direction, i.e., the spin exchange between the NN Cu atoms along the chains with the shortest Cu . . . Cu distance of 3.556 Å [27–29]. However, Vasil’ev *et al.* already estimated the intrachain exchange J and interchain spin exchange J' to be 68 K and 33 K, respectively, leading to a very large value for the ratio $J'/J \approx 0.5$ [27]. Kikuchi *et al.* stated that a pure 1D chain model provides a poor description of α - CuV_2O_6 because of the large value for J'/J , and hence cannot explain the relatively high AFM ordering temperature of ~ 23 found by AFM resonance [27], neutron-powder diffraction, and NMR experiments [28] as well as specific-heat capacity measurements [29]. This view was also echoed by Prokofiev *et al.*, who pointed out the need to treat α - CuV_2O_6 as an anisotropic 3D rather than a 1D magnetic material [29].

A detailed inspection of the crystal structure of α - CuV_2O_6 (see Table S1 in the Supplemental Material [35] for structure

details), and especially of the orientation of the Jahn-Teller elongated CuO_6 octahedra, reveals that the CuO_4 equatorial plane of the Cu^{2+} cations with the four closest oxygen atoms at distances of 1.91 Å and 2.04 Å is inclined with respect to the propagation direction ([100]) of the ribbon chains [see Fig. 1(a)]. As already noted by Koo and Whangbo, such an arrangement of the magnetic $d_{x^2-y^2}$ orbitals suppresses the Cu–O–Cu spin exchanges, unless both Cu–O bonds lie in the CuO_4 equatorial planes containing the $d_{x^2-y^2}$ magnetic orbitals [36]. This observation presents serious issues concerning the spin lattice relevant for α - CuV_2O_6 . The 1D chain of edge-sharing, axially elongated CuO_6 octahedra shown in Fig. 1(a) becomes a stack of isolated CuO_4 square planes once the elongated Cu–O bonds are removed to highlight only the CuO_4 planes containing the magnetic orbitals. Such stack chains are isolated from each other in α - CuV_2O_6 [see Figs. 1(b) and 1(c)], so there is no spin exchange of the Cu–O–Cu type (superexchange) in α - CuV_2O_6 . Thus, the magnetic properties of α - CuV_2O_6 have to be determined by spin exchanges of the Cu–O . . . O–Cu super-superexchange type, in which both Cu–O bonds lie in the CuO_4 planes containing the $d_{x^2-y^2}$ magnetic orbitals even if the two Cu^{2+} ions do not share a common oxygen atom. Such spin exchanges are mostly AFM in nature and can be strong when the O . . . O contact distance lies within the van der Waals (vdW) distance (~ 3.0 Å) and when the Cu–O . . . O angles are large. This is so because the magnetic orbital, commonly referred to as the $\text{Cu } x^2-y^2$ orbital, has the $2p$ orbitals of the O ligands combined out of phase with the $\text{Cu } x^2-y^2$ orbital and because the strength of the Cu–O . . . O–Cu spin exchange is determined by how strongly these O $2p$ orbitals overlap across the O . . . O contact [5,6]. When the O . . . O contact is intervened by a d^0 metal cation such as V^{5+} , the strength of the Cu–O . . . V^{5+} . . . O–Cu exchange is influenced by the empty d orbitals of the V^{5+} cation [37–39].

To find the correct spin lattice we have carried out extensive spin-polarized density-functional theory (DFT + U) calculations for several magnetic configurations (see Fig. S5 in the Supplemental Material for details [35]) and mapped their relative energies to the corresponding relative energies expected from the spin Hamiltonian. We find that the magnetic properties of α - CuV_2O_6 need to be described by a spin $S = 1/2$ Heisenberg rectangular spin lattice defined by J_c and J_{a+b} with $J_c/J_{a+b} \sim 0.7$ (see Figs. 11 and 12 for details). Our theoretical finding, which clarifies the origin of the observations by Vasil’ev *et al.* [27], Kikuchi *et al.* [28], and Prokofiev *et al.* [29] that α - CuV_2O_6 is not a 1D magnetic system, is corroborated by a conclusive magnetic structure determination from high-intensity neutron-diffraction measurements as well as the anisotropic magnetization and magnetic susceptibility data. In agreement with the theoretical results, we indeed observe that the spin exchange between NN Cu moments along the propagation direction of the ribbon chains is not AFM but FM and by a factor of ~ 30 weaker than the strongest AFM exchange across the interconnecting VO_6 double chains. A comparison of the temperature dependence of the magnetic susceptibilities with quantum Monte Carlo calculations (QMC) for the Heisenberg rectangular spin lattice confirms the anisotropy ratio derived from the DFT calculations.

II. EXPERIMENTAL DETAILS

Polycrystalline samples of α -CuV₂O₆ were synthesized by firing CuO (99.999%, Alfa Aesar) and V₂O₅ (99.999%, Alfa Aesar) in a porcelain crucible. In a first step, the thoroughly mixed powder was annealed to 540 °C, then ground again in an agate mortar and heated to 610 °C [40]. Crystals of α -CuV₂O₆ were grown from the powder by chemical vapor phase transport (CVT) in a temperature gradient from 600 °C to 500 °C using TeCl₄ as a transport agent. The powder samples were initially characterized with respect to phase purity by x-ray powder diffraction at room temperature using MoK α ₁ radiation. High-resolution neutron powder diffraction patterns were collected at 1.5 K on the high-resolution two-axis diffractometer D2B installed at the Institut Laue-Langevin (ILL, Grenoble) using neutrons of 1.594 Å wavelength. The sample of \sim 9 g was filled into a thin-walled vanadium tubular container of 8-mm outer diameter. Rietveld refinements by varying the lattice parameters and atom positions were performed in the triclinic space group $P-1$ (No. 2) using the FULLPROF software package assuming a pseudo-Voigt peak profile (FULLPROF NPR = 5) [42]. Isotropic and anisotropic displacement parameters were tested in case of the x-ray and neutron diffraction patterns, respectively. The background was modeled by a higher-order Chebychev polynomial. The refinements typically converged to Bragg- and R_f -reliability factors of \sim 2% or less and χ^2 -values better than 1 were achieved for the x-ray patterns. For the neutron diffraction, the reliability factors were somewhat larger (see Table SI in the Supplemental Material [35] for more structure details). Medium-resolution high-intensity neutron powder diffraction was performed between 1.5 K and 30 K on ILL's diffractometer D20 at a wavelength of 2.42 Å. DC magnetization measurements versus magnetic field and temperature were performed in a Magnetic Property Measurement System employing the RSO option (Quantum Design, MPMSXL). The needle-shaped crystals were oriented with the a axis ($P-1$ setting, needle axis) parallel and perpendicular to the magnetic field. Heat-capacity measurements on a crystal grown in a V₂O₅-K₂SO₄ melt [29] as well as on a CVT crystal were performed in a physical property measurement system (Quantum Design, PPMS) in magnetic fields up to 9 T with the field oriented perpendicular to the crystal needles.

III. RESULTS

A. Magnetic and thermal properties

The magnetic susceptibility of polycrystalline samples of α -CuV₂O₆ has been reported and discussed before by Vasil'ev *et al.*, Kikuchi *et al.*, and Prokofiev *et al.* [27–29]. They consistently reported a Néel temperature of \sim 24 K which was also found in first measurement of the heat capacity by Prokofiev *et al.* [29]. Whereas Vasil'ev *et al.* and Kikuchi *et al.* found reasonable agreement of their experimental magnetic susceptibility data with the Bonner-Fisher model for a 1D spin $S = 1/2$ Heisenberg chain [43]; Prokofiev *et al.* reported discrepancies. Especially the g factor obtained from their fit of a 1D Heisenberg model to the susceptibilities measured with magnetic field along the needles (b axis in $C-1$ setting, a axis in $P-1$ setting) amounted to 2.44, remarkably larger

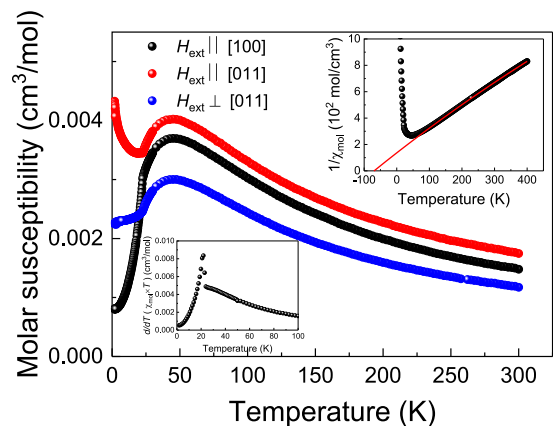


FIG. 2. Anisotropy of the magnetic susceptibilities of a crystal of α -CuV₂O₆ observed with magnetic field applied parallel [100] (along the crystal needle) and perpendicular as indicated. The upper inset displays a Curie-Weiss plot of the inverse susceptibility. The lower inset shows Fisher's heat capacity [45] obtained by taking the derivative with respect to temperature of the quantity $\chi_{\text{mol}} \times T$, showing the long-range ordering anomaly at 22.2(1) K.

than is typically observed for Cu²⁺ in Jahn-Teller elongated octahedral environment [44]. Figure 2 displays the temperature dependence of the magnetic susceptibilities of a needle-shaped crystal of α -CuV₂O₆ with the external field oriented parallel (parallel a in $P-1$ setting, parallel b in $C-1$ setting) and perpendicular to the crystal needle, as indicated. As described before for polycrystalline samples, the susceptibilities are characterized by a broad maximum centered at about 43 K due to short-range AFM ordering, followed by a Curie-Weiss-type hyperbolic decrease above. The Curie-Weiss temperature amounts to $-70(2)$ K, (see inset in Fig. 2), indicating predominant AFM spin exchange. For the crystal sample, we observe a large directional dependence of the magnetic susceptibilities. Not only are the susceptibilities different in magnitude, indicating a substantial anisotropy of the effective moments viz. the g factors in the different directions but, especially, the temperature dependence below the short-range-order maximum is different for the three perpendicular field directions. Whereas, with a field applied along [100], the susceptibility continuously decreases to lowest temperatures, the susceptibilities with a field applied perpendicular to [100] (perpendicular to the crystal needles) initially drop and, after a kink at \sim 22.5 K, either level off or slightly increase again. The kink with the change of the slope for $\chi_{\text{mol}}([100])$ and a sharp anomaly in the quantity $d/dT(\chi_{\text{mol}} \times T)$ (Fisher's heat capacity) [45] marks the onset of AFM long-range order, in agreement with preceding results [27–29]. The anisotropy of the single-crystal susceptibilities is typical for an uniaxial antiferromagnet with the easy axis aligned along [100]. Figure 3 displays the isothermal magnetization of a needle-shaped α -CuV₂O₆ crystal at 1.85 K with the external field oriented parallel ($\parallel a$ in $P-1$ setting, $\parallel b$ in $C-1$ setting) and perpendicular to the needle axis. With the latter orientation, the magnetization increases linearly with the field, whereas with the field oriented along the needle we observe a spin-flip of the magnetization, suggesting that the magnetic field was oriented along or close to the easy axis.

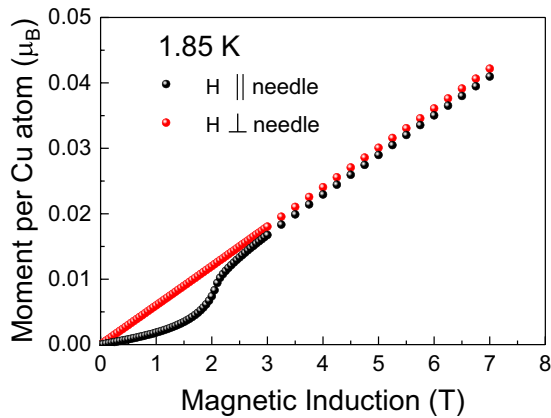


FIG. 3. Isothermal magnetization of a α - CuV_2O_6 crystal at 1.85 K with the magnetic field applied parallel and perpendicular to the crystal needle as indicated.

The spin-flop field versus temperature determined from the derivatives of the isothermal magnetization $M_{\text{mol}}(T, H)$, $(dM_{\text{mol}}(H, T)/dH)_T$ is summarized in Fig. 4, where the inset highlights the temperature dependence of the peaks. The spin-flop upshifts with field when increasing the temperature and disappears above the Néel temperature.

Figure 5 displays the temperature and magnetic field dependence of the heat capacity near the Néel temperature of two crystals of different origins. The magnetic field was oriented perpendicular to the needle-shaped crystals. The λ anomaly in the heat capacity of the crystal grown from the flux is well shaped and sharp and at zero field peaks at 22.44(4) K. Applying a magnetic field slightly increases the Néel temperature (see inset Fig. 5) but does not alter the shape of the anomaly. The magnetic anomaly in the heat capacity of the CVT crystal exhibits the same onset temperature but is broadened, possibly due to some inhomogeneity.

B. Magnetic structure

The magnetic structure of α - CuV_2O_6 was determined from neutron-powder-diffraction patterns. Figure 6 displays the

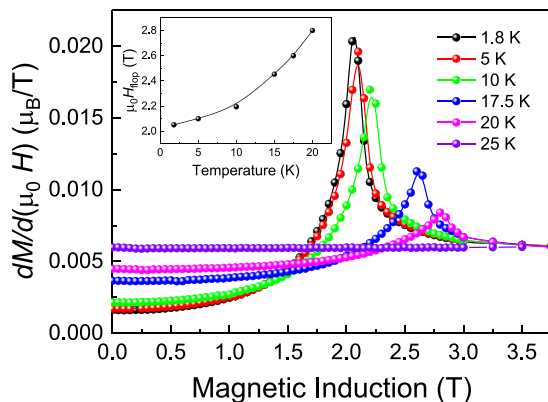


FIG. 4. Derivative of the isothermal magnetization (per Cu atom) with respect to the magnetic field indicating the position of the spin flop. The inset provides the spin-flop field versus measuring temperature.

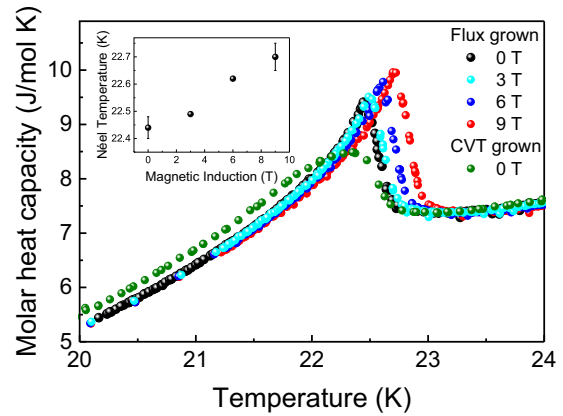


FIG. 5. Heat capacity versus magnetic field of a flux grown and a CVT-grown crystal near the Néel temperature. The λ -shaped anomaly shifts to higher temperature with increasing field applied perpendicular to the crystal needle. The anomaly of the CVT-grown crystal is somewhat smeared out, however, with the same onset temperature as the flux-grown crystal. The magnetic entropy contained in the anomaly amounts to $\sim 2\%$ of $R \ln 2$ expected for a spin $S = 1/2$ system, implying that almost all magnetic entropy is removed by short-range AFM ordering above the Néel temperature.

diffraction pattern taken at 1.5 K together with a Rietveld profile refinement of the nuclear structure with atom and lattice parameters in agreement with those derived from the high-resolution neutron data (see Table SI in the Supplemental Material [35] for more structure details). At $2\Theta = 16.14^\circ$ ($d = 8.61 \text{ \AA}$), an extra Bragg reflection is observed. It disappears above $\sim 22 \text{ K}$, indicating that it is of magnetic origin (see Fig. 7). To search for more magnetic Bragg reflections,

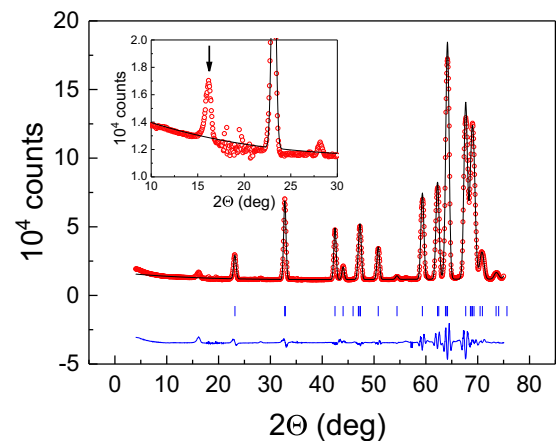


FIG. 6. Neutron-powder-diffraction pattern of α - CuV_2O_6 collected at 1.5 K using neutrons with a wavelength of $\lambda = 2.424 \text{ \AA}$ on ILL's medium resolution high-intensity powder diffractometer D20 shown together with a Rietveld profile refinement of the nuclear structure (solid black line). The red circles represent the measured counts, the blue solid line at the bottom of the graphs shows the difference between the observed and calculated patterns. Vertical ticks (blue) mark the Bragg angles of the reflections used to simulate the refined patterns. The inset displays the range with the strongest magnetic Bragg reflection marked by the arrow at $d = 8.61 \text{ \AA}$ in an enlarged scale.

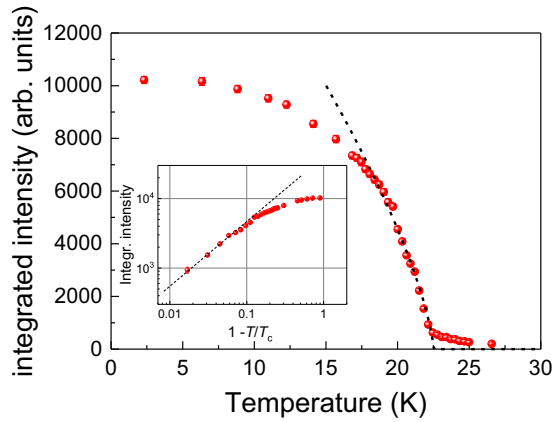


FIG. 7. Red circles: Integrated intensities of the magnetic Bragg reflection observed at $2\Theta = 16.14^\circ$. The dashed line is a fit of the data close to $T_c = 22.37$ K with a critical power law according to Eq. (1), assuming a critical exponent $\beta = 0.36$.

we used a contour plot of difference patterns collected while ramping up the temperature from 1.5 K to 30 K. As can be seen from Fig. 8, five additional Bragg peaks can be identified, two of them above 40° being very weak. The plot of the integrated intensity of the 16.14° magnetic Bragg reflection as a function of temperature confirms the second-order nature of the phase transition. A fit of the integrated intensity, $I(T)$, to a power law assuming a critical exponent $\beta = 0.36$, typically found for the 3D-Heisenberg universality class [46],

$$I(T) \propto (1 - T/T_c)^{2\beta}, \quad (1)$$

yields a critical temperature of

$$T_c = 22.37(7) \text{ K},$$

in good agreement with the critical temperature found from the magnetization and heat capacity experiments.

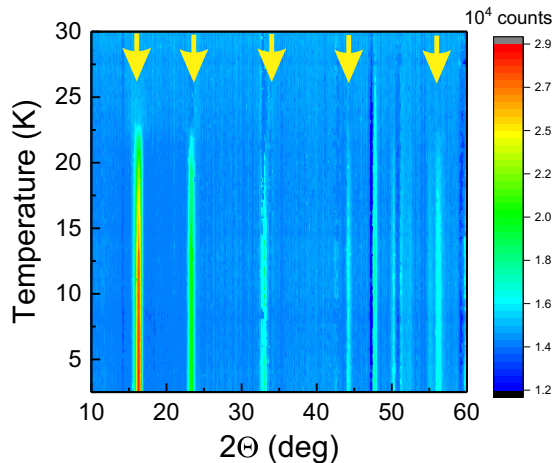


FIG. 8. Contour plot of the difference intensity (30 K data set subtracted) as a function of the Bragg angle and temperature of the D20 neutron-powder-diffraction patterns ($\lambda = 2.424$ Å) highlighting the magnetic Bragg reflections marked by (yellow) vertical arrows. They disappear above ~ 23 K.

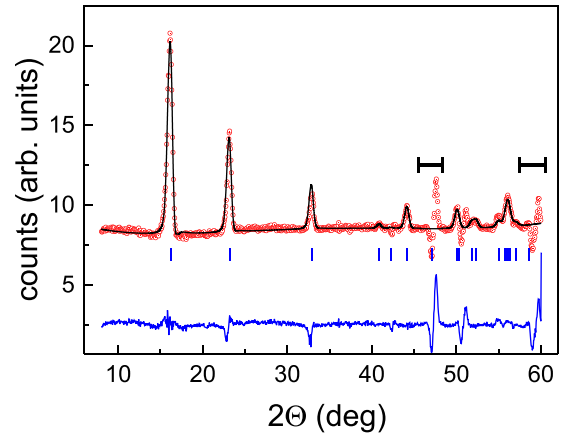


FIG. 9. Rietveld profile refinement of the difference pattern, 1.5 K–30 K. Red: Circles indicate the difference counts and the (black) solid line shows the theoretical pattern calculated using the Bragg angles of the magnetic reflections indicated by the (blue) vertical bars. The (blue) solid line marks the difference between measured and calculated intensity. The two horizontal (black) short bars indicate regions which were excluded in the refinement.

Using the program *k-search* contained in the FULLPROF suite [42] and the lattice parameters refined from the 1.5 K refined nuclear pattern (cf. Fig. 6) the magnetic Bragg reflection could be readily indexed based on the propagation vector (*P*-1 setting of space group No. 2):

$$\vec{\tau} = (0, 0.5, 0.5).$$

A symmetry analysis with the program BasIreps [47,48] yielded two equivalent 1D irreducible representations with real basis vectors along *a*, *b*, and *c*. A full least-squares refinement of the magnetic structure was finally carried out based on the difference pattern $I(1.5 \text{ K}) - I(30 \text{ K})$ augmented by a constant offset to avoid small negative differences. Figure 9 shows the refined difference pattern and Fig. 10 displays the magnetic structure. As already implied by the propagation vector, one finds a doubling of the nuclear cell along *b* and *c*, with the magnetic moments aligned essentially along the

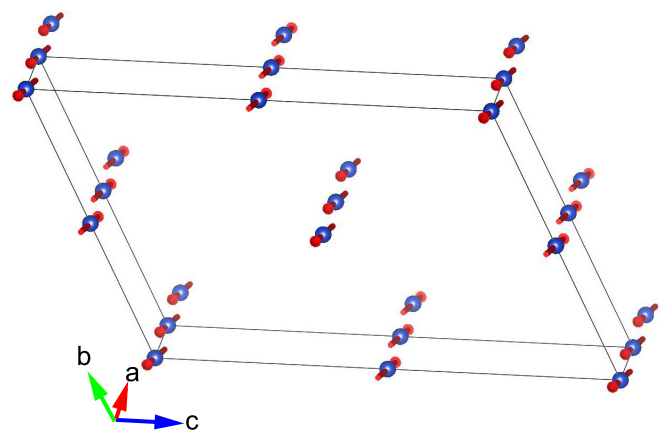


FIG. 10. Magnetic structure of α -CuV₂O₆. The moments point essentially along the *a* axis (*P*-1 setting of space group No. 2).

a axis and vanishing component along b . Allowing a small component of the moment pointing along b [$\approx 0.05(3)\mu_B$] did not significantly improve the fits. The magnitude of ordered moment amounts to

$$\mu = 0.66(2)\mu_B,$$

in good agreement with the results of our DFT calculations and with Kikuchi *et al.*'s finding [28].

The refined components of the ordered moment are

$$\mu(a) = 0.65(1)\mu_B,$$

$$\mu(b) = 0.0\mu_B,$$

$$\mu(c) = 0.12(3)\mu_B.$$

Antiparallel collinear alignment of the Cu moments is found along the b and the c lattice directions, whereas along the a axis (chain direction) collinear parallel alignment is observed.

IV. DISCUSSION

Magnetic structure

Our magnetic structure solution for α -CuV₂O₆ based on a total of five magnetic Bragg reflections is essentially a C -type AFM structure characterized by a FM alignment of the Cu moments along the [100] (P -1 setting) direction, i.e., the direction of the closest Cu...Cu approach. Cu moments in neighboring chains in the a - b plane align antiparallel to those in neighboring chains along the [001] direction. Our magnetic structure solution agrees with Kikuchi *et al.*'s second magnetic structure proposal shown as Fig. 9(B) in Ref. [28]. The saturation moment refined for the Cu atoms is $0.66\mu_B$ close to $0.7\mu_B$ proposed by Kikuchi and the DFT calculations (see below). The FM alignment of the Cu moment along [100], which is counterintuitive to the 1D AFM character of α -CuV₂O₆ surmised by all previous studies [27–29], is surprising.

V. DFT CALCULATIONS OF THE SPIN EXCHANGE INTERACTIONS

To establish the spin-exchange paths and to resolve the apparent discrepancies between our study and other reports concerning α -CuV₂O₆, we first analyzed the crystal structure of α -CuV₂O₆ from the viewpoint of “square-planar” CuO₄ units. For each axially elongated CuO₆ octahedron, the x^2-y^2 magnetic orbital of the Cu²⁺ ion is contained in the CuO₄ plane made up of the four short, equatorial Cu–O bonds [34,35]. As already sketched in the Introduction, the NN spin exchange J_a along the a direction [see Fig. 1(a)] should be negligible since its O...O distance (3.556 Å) is longer than the vdW distance, and so should be the NN spin exchange J_b along the b direction [Fig. 1(c)] for the same reason (O...O = 4.956 Å) (see Table I for more geometrical details). Consequently, Cu–O...O–Cu-type super-superoxchange has to be considered to describe the magnetic properties of α -CuV₂O₆. α -CuV₂O₆ has two Cu–O...O–Cu spin-exchange paths with O...O contact shorter than the vdW distance; the NN exchange J_c along the c direction with O...O = 2.738 Å [Fig. 11(a)], and the NN exchange J_{a+b} along

TABLE I. Geometrical parameters associated with the spin-exchange paths J_a , J_{a+b} , J_b , and J_c used in the mapping analysis.

		Cu ... Cu (Å)	O ... O (Å)	Other
J_a	$\parallel a$	3.556	3.556	parallel CuO ₄ planes
J_{a+b}	$\parallel (a+b)$	4.858	2.665	O...V ⁵⁺ ...O bridges
J_b	$\parallel b$	4.956	4.956	parallel CuO ₄ planes
J_c	$\parallel c$	6.455	2.738	$\angle\text{Cu-O...O} = 161.07^\circ$

the $(a+b)$ direction with O...O = 2.665 Å [see Fig. 11(b)]. One might speculate whether J_{a+b} is stronger than J_c since it has a shorter O...O distance. However, the Cu–O...O angles are considerably greater in the exchange path J_c (161.07°) than in the J_{a+b} path (131.98°, 96.29°), leading to the opposite speculation. Another complicating factor is that there is no intervening V⁵⁺ cation in the O...O contact of J_c [Fig. 11(a)], but there is in each O...O contact of J_{a+b} . The empty d orbitals of the d^0 cation V⁵⁺ can influence the strength of the Cu–O...O–Cu exchange even when the Cu–O...O angles are not large because the interaction between the O $2p$ orbitals across each O...O contact can be modified by empty d orbitals of V⁵⁺ [6]. Consequently, the spin lattice relevant for α -CuV₂O₆ would be a two-dimensional (2D) rectangular lattice [see Fig. 11(c)] if the J_c and J_{a+b} exchanges are comparable in strength, but would be a 1D chain otherwise. Note that the CuO₄ stack-chains lying in every plane parallel to the ab plane are bridged by the VO₄ tetrahedra to form a layer of composition CuV₂O₆ [see Fig. 11(d)]. Thus, the

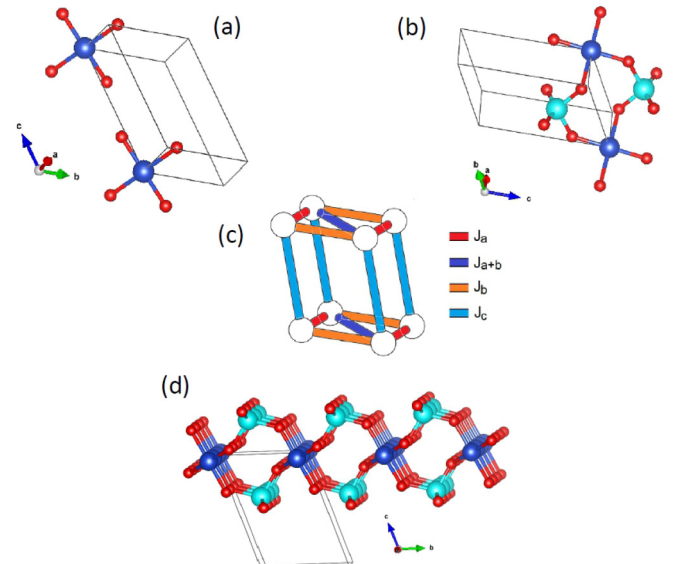


FIG. 11. Structural features of α -CuV₂O₆ associated with its spin-exchange paths. (a) Two NN CuO₄ planes along the c direction defining the J_c exchange path; (b) two NN CuO₄ planes along the $(a+b)$ direction defining the J_{a+b} exchange path, where the Cu²⁺ cations are bridged by two VO₄ tetrahedra; (c) Four spin-exchange paths of α -CuV₂O₆ presented in a unit cell box. (d) A perspective view of a single CuV₂O₆ layer parallel to the ab -plane. Color coded as in Fig. 1.

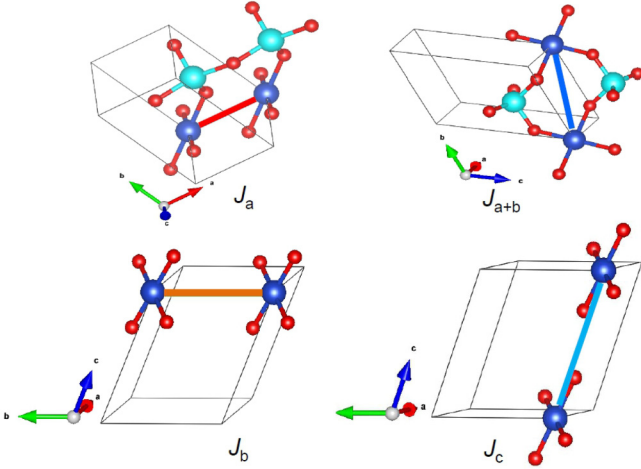


FIG. 12. Relevant spin-exchange paths, J_a , J_{a+b} , J_b , and J_c , in α -CuV₂O₆. Color coded as in Fig. 1. The exchange paths for J_a , J_{a+b} , J_b , and J_c are represented by red, blue, orange, and cyan lines, respectively.

exchange paths J_{a+b} are present within each CuV₂O₆ layer while the paths J_c occur between two adjacent CuV₂O₆ layers.

To verify this point, we have carried out spin-polarized DFT + U calculations for a set of eight collinear ordered spin structures (Fig. S5) considering the spin-exchange paths J_a , J_{a+b} , J_b , and J_c , which are the NN spin exchanges along the a , $(a+b)$, b , and c directions, respectively (see Table I for the geometrical details). The relative energies obtained for these states from the spin-polarized DFT calculations were mapped onto the corresponding relative energies of the spin Hamiltonian written in terms of the four spin-exchange paths, J_a , J_{a+b} , J_b , and J_c highlighted in Fig. 12.

The results of the mapping analysis of the total energies Table SIII [35] to Eqs. (S2) [35] are summarized in Table II.

Table II reveals that the J_a is weakly FM, J_b is weakly AFM, while J_{a+b} and J_c are strongly AFM. Thus, as anticipated from the examination of the crystal structure, J_{a+b} and J_c , are much stronger than J_a and J_b with the J_c/J_{a+b} ratio of ~ 0.8 . The J_{a+b} path lies within each CuV₂O₆ layer [Fig. 11(d)]. In contrast, the J_c path occurs between two adjacent CuV₂O₆ layers [Fig. 11(a)]. Thus, α -CuV₂O₆ must be described by a 2D rectangular spin lattice defined by the two

TABLE II. J_a , J_{a+b} , J_b , and J_c spin exchange parameters for α -CuV₂O₆ determined by the energy-mapping analysis based on the DFT+ U calculations using $U_{\text{eff}} = 4, 5$, and 6 eV. The Curie-Weiss temperature θ_{CW} given in the last row has been calculated according to $\theta_{\text{CW}} = -2/3 \times S(S+1) \sum_{i=1}^4 J_i$.

$U_{\text{eff}} =$	4 eV	5 eV	6 eV
	Spin exchange (meV)		
J_a	-0.23(13)	-0.23(8)	-0.29(6)
J_{a+b}	7.48(13)	6.06(9)	4.85(6)
J_b	0.18(11)	0.08(8)	0.10(6)
J_c	6.55(16)	5.15(10)	3.94(8)
J_c/J_{a+b}	0.88(4)	0.85(3)	0.81(3)
$\theta_{\text{CW}}/\text{K}$	-81	-64	-50

TABLE III. Magnetic moments on the Cu, V and O atoms in the FM states of α -CuV₂O₆ from the DFT+ U calculations.

Atom	μ_B/atom		
	$U_{\text{eff}} = 4$ eV	5 eV	6 eV
Cu	0.68	0.71	0.74
V	0.03	0.03	0.02
O	0.04	0.04	0.03

repeat vectors along the c and $(a+b)$ directions. Structurally, however, the CuV₂O₆ layers lie in the ab plane.

The DFT + U calculations of the ordered spin states show that they are all magnetic insulating states with the magnetic moments essentially residing on the Cu²⁺ ions. The moments amount to 0.69–0.74 μ_B (see Table III) in good agreement with our experimental findings. Our magnetic structure solution agrees with the second structure proposed by Kikuchi *et al.* (see Ref. [28], Fig. 9 B). The moment arrangement of our magnetic structure AFM7 (i.e., C-type AFM) is depicted schematically in Fig. 13 (right-hand side). Its calculated exchange energies with respect to the FM structure are listed in Table SIII of the Supplemental Material [35]. Also shown in Fig. 13 (left-hand side) is the alternative magnetic structure (A-type AFM) proposed by Kikuchi *et al.*. Using the spin-exchange parameters of Table II, we find that the total exchange energy of the C-type AFM structure is more stable than the A-type AFM structure by 29.7, 23.6, and 18.6 meV per $2a \times 2b \times 2c$ supercell for $U_{\text{eff}} = 4, 5$, and 6 eV, respectively, clearly showing that our magnetic structure, AFM7, is energetically more favorable.

Two-dimensional spin lattice

The magnetic structure determination lends strong support for the results of our DFT + U calculations, which suggest a 2D rectangular spin lattice model. This result questions all evaluations of the magnetic susceptibility data carried out so far assuming a Heisenberg 1D chain with uniform AFM NN spin-exchange interaction along the octahedral chains [27–29]. We have therefore reanalyzed the magnetic susceptibility data in terms of a spin $S = 1/2$ Heisenberg rectangular spin lattice model. Using QMC calculations, we examined the temperature dependence of the magnetic susceptibility and the heat capacity for the spin $S = 1/2$ Heisenberg rectangular spin lattice model as a function of the ratio $\alpha = J_y/J_x$ from $0.5 \leq \alpha \leq 1$ (see Supplemental Material [35] for more

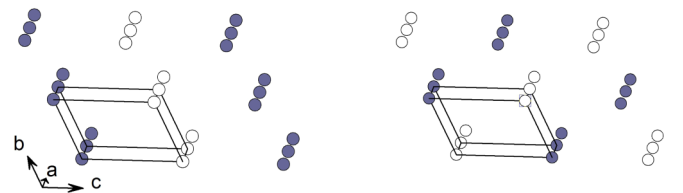


FIG. 13. Schematic representations of the two magnetic structures of α -CuV₂O₆ proposed by Kikuchi *et al.* Left: Figure 9 A of Ref. [28]. Right: Figure 9 B of Ref. [28]. The latter is identical to our magnetic structure solution.

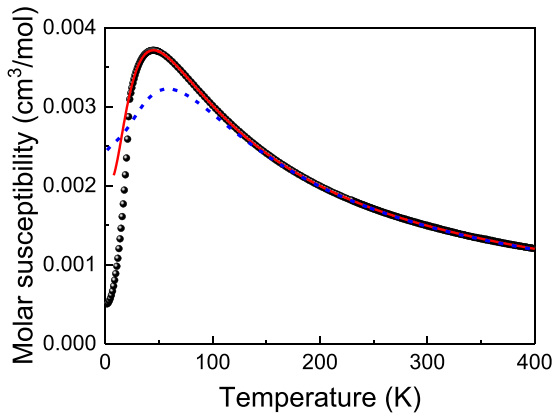


FIG. 14. Magnetic susceptibility of a crystal of α -CuV₂O₆ measured with a field of 0.1 Tesla applied along the crystal needle (a axis in P -1 setting). The (red) solid line is a fit of the magnetic susceptibilities ($T \geq 30$ K) to the prediction of a spin $S = 1/2$ Heisenberg rectangular lattice with spin exchange parameters given in the text. In addition to the spin susceptibility, according to Eq. (2) a temperature-independent susceptibility $\chi_0 = 130(2) \times 10^{-6} \text{cm}^3/\text{mol}$ to account for the diamagnetic susceptibilities of the electrons in the closed electron shells and van Vleck contributions was added [10]. The blue dashed line shows the theoretical susceptibility of a spin $S = 1/2$ AFM Heisenberg chain with uniform NN exchange interaction of 90 ± 3 K using the same g factor [49].

details). The results for six discrete ratios of α are subsequently fitted to a Padé approximant, adopting the procedure described in detail in Ref. [49]. The Padé coefficients for the discrete α values were fitted to a fourth-degree polynomial. This enables continuous interpolation of the anisotropy ratio α when fitting experimental data. Also taking a temperature independent susceptibility and a Curie-Weiss-type impurity term into account, we fit the experimental susceptibility data using the equation

$$\chi_{\text{mol}}(T) = (1 - x_{\text{imp}}) \chi_{\text{sq}}^*(\alpha, g, T) + x_{\text{imp}} C_{\text{imp}} / (T - \Theta) + \chi_0, \quad (2)$$

where the first term on the right-hand side represents the susceptibility of the rectangular model including interplanar coupling in a mean-field approach (see below), and the second and third terms account for paramagnetic impurities and a temperature independent susceptibility, respectively. x is the fraction of paramagnetic impurities. Figure 14 shows the fit of the magnetic susceptibility of α -CuV₂O₆ with field aligned along [100].

Using $g_{[100]} = 2.297(2)$, close to the value observed in the ESR experiments (see Figs. S7 and S8 in the Supplemental Material [35]), the fits indicate the following parameters for J_{a+b} and the ratio α :

$$J_{a+b} = 54.6(5)\text{K},$$

$$J_c/J_{a+b} = 0.71(1),$$

in good agreement with the predictions from the DFT + U calculations. The temperature-independent susceptibility χ_0 amounts to

$$\chi_0 = 130(2) \times 10^{-6} \text{cm}^3/\text{mol},$$

somewhat larger than typically expected from the sum of the diamagnetic and van Vleck contributions [10].

Long-range AFM order in α -CuV₂O₆ takes place at 22.4 K due to interplanar spin exchange coupling. When fitting the experimental susceptibilities to Eq. (2), in addition to the ratio α and the g factor, a weak interplanar exchange interaction, J_{inter} , was considered by a mean-field approach according to

$$\chi_{\text{sq}}^*(\alpha, g, T) = \chi_{\text{sq}}(\alpha, g, T) / [1 + \chi_{\text{sq}}(\alpha, g, T) \times (z_{\text{inter}} J_{\text{inter}}) / (N_A g^2 \mu_B^2)],$$

with z_{inter} being the number of neighboring moments seen by a Cu moment in an adjacent plane. J_{inter} represents the spin-exchange interaction between planes and N_A is Avogadro's constant [50]. Commonly, one uses the product $z_{\text{inter}} J_{\text{inter}}$, representing an effective interplanar coupling strength which, according to the fits, amounted to

$$z J_{\text{inter}} = 2.9(1) \text{ K} (\equiv 0.25(1) \text{ meV}).$$

The interplanar spin-exchange parameters are given by J_a and J_b with $z = 2$ neighbors for each. Taking the values for J_a and J_b from Table II for $U_{\text{eff}} = 6$ eV, the interplanar spin exchange adds up to 0.38 meV, consistent with this finding.

VI. SUMMARY AND CONCLUSION

α -CuV₂O₆ has previously been analyzed in terms of a 1D AFM Heisenberg spin $S = 1/2$ model with uniform NN spin-exchange interaction. The results presented here clearly reveal that α -CuV₂O₆ rather constitutes a 2D spin $S = 1/2$ Heisenberg rectangular lattice with a spin-exchange ratio of $J_c/J_{a+b} \sim 0.7$. The spin exchange along the infinite octahedral chains propagating along a , which had been regarded as dominant and AFM in all previous studies, is negligibly weak. This finding reflects the fact that any Cu–O–Cu spin exchange is negligible unless both Cu–O bonds lie in the CuO₄ planes containing the magnetic orbitals of the Cu²⁺ ions. According to our heat capacity, magnetization, and neutron-diffraction measurements, α -CuV₂O₆ undergoes long-range AFM order below ~ 22.4 K to a C -type AFM structure. The magnetic moments on the Cu ions are reduced and amount to $\sim 0.66 \mu_B$. The crystal structure exhibits noticeable magnetoelastic coupling (see Figs. S2 and S3 in the Supplemental Material [35]) when AFM order sets in. α -CuV₂O₆ constitutes a striking example where the combination of *ab initio* and model-based calculations and experimental data are decisive for a conclusive assignment of the correct spin lattice of a low-dimensional quantum antiferromagnet.

ACKNOWLEDGMENTS

L.W. and S.W. acknowledge support by the Deutsche Forschungsgemeinschaft (DFG) through Grant No. WE/3649/4-2 of the FOR 1807 and through RTG 1995. Furthermore, we thank the IT Center at RWTH Aachen University and the JSC Jülich for access to computing time through JARA-HPC. We Thank E. Brücher and S. Höhn for substantial experimental assistance.

- [1] S. Sachdev, *Quantum Phase Transitions* (Cambridge University Press, Cambridge, New York, 1999).
- [2] L. Balents, *Nature* **464**, 199 (2010).
- [3] C. Lacroix, P. Mendels, and F. Mila, *Introduction to Frustrated Magnetism* (Springer, Heidelberg, 2011).
- [4] L. Savary and L. Balents, *Rep. Prog. Phys.* **80**, 016502 (2017).
- [5] M. Whangbo, H. Koo, and D. Dai, *J. Solid State Chem.* **176**, 417 (2003).
- [6] H. J. Xiang, C. Lee, H.-J. Koo, X. G. Gong, and M.-H. Whangbo, *Dalton Trans.* **42**, 823 (2013).
- [7] B. J. Gibson, R. K. Kremer, A. V. Prokofiev, W. Assmus, and G. J. McIntyre, *Physica B* **350**, e253 (2004).
- [8] M. Enderle, C. Mukherjee, B. Fåk, R. K. Kremer, J.-M. Broto, H. Rosner, S.-L. Drechsler, J. Richter, J. Malek, A. Prokofiev, W. Assmus, S. Pujol, J.-L. Raggazzoni, H. Rakoto, M. Rheinstädter, and H. M. Rønnow, *Europhys. Lett.* **70**, 237 (2005).
- [9] L. Capogna, M. Mayr, P. Horsch, M. Raichle, R. K. Kremer, M. Sofin, A. Maljuk, M. Jansen, and B. Keimer, *Phys. Rev. B* **71**, 140402(R) (2005).
- [10] M. G. Banks, R. K. Kremer, C. Hoch, A. Simon, B. Ouladdiaf, J.-M. Broto, H. Rakoto, C. Lee, and M.-H. Whangbo, *Phys. Rev. B* **80**, 024404 (2009).
- [11] J. M. Law, P. Reuvekamp, R. Glaum, C. Lee, J. Kang, M.-H. Whangbo, and R. K. Kremer, *Phys. Rev. B* **84**, 014426 (2011).
- [12] S. Lebernegg, A. A. Tsirlin, O. Janson, R. Nath, J. Sichelschmidt, Yu. Skourski, G. Amthauer, and H. Rosner, *Phys. Rev. B* **84**, 174436 (2011).
- [13] C. Lee, Jia Liu, M.-H. Whangbo, H.-J. Koo, R. K. Kremer, and A. Simon, *Phys. Rev. B* **86**, 060407(R) (2012).
- [14] K. Caslin, R. K. Kremer, F. S. Razavi, A. Schulz, A. Muñoz, F. Pertlik, J. Liu, M.-H. Whangbo, and J. M. Law, *Phys. Rev. B* **89**, 014412 (2014).
- [15] A. Vasil'ev, O. Volkova, E. Zvereva, and M. Markin, *npj Quantum Mater.* **3**, 18 (2018).
- [16] J. B. Goodenough, *Magnetism and the Chemical Bond*, (Interscience, New York, 1963)
- [17] J. Kanamori, *J. Appl. Phys. Suppl.* **31**, 14S (1960).
- [18] P. W. Anderson, *Phys. Rev.* **115**, 2 (1959).
- [19] Y. Naito, K. Sato, Y. Yasui, Y. Kobayashi, and M. Sato, *J. Phys. Soc. Jpn.* **76**, 023708 (2007).
- [20] F. Schrettle, S. Krohns, P. Lunkenheimer, J. Hemberger, N. Büttgen, H.-A. Krug von Nidda, A. V. Prokofiev, and A. Loidl, *Phys. Rev. B* **77**, 144101 (2008).
- [21] L. Zhao, T.-L. Hung, C.-C. Li, Y.-Y. Chen, M.-K. Wu, R. K. Kremer, M. G. Banks, A. Simon, M.-H. Whangbo, C. Lee, J. S. Kim, I. Kim, and K. H. Kim, *Adv. Mater.* **24**, 2469 (2012).
- [22] M. E. Zhitomirsky and H. Tsunetsugu, *Europhys. Lett.* **92**, 37001 (2010).
- [23] L. E. Svistov, T. Fujita, H. Yamaguchi, S. Kimura, K. Omura, A. Prokofiev, A. I. Smirnov, Z. Honda, and M. Hagiwara, *JETP Letters* **93**, 21 (2011).
- [24] Y. Yasui, Y. Naito, K. Sato, T. Moyoshi, M. Sato, and K. Kakurai, *J. Phys. Soc. Jpn.* **77**, 023712 (2008).
- [25] M. Mourigal, M. Enderle, B. Fåk, R. K. Kremer, J. M. Law, A. Schneidewind, A. Hiess, and A. Prokofiev, *Phys. Rev. Lett.* **109**, 027203 (2012).
- [26] A. Orlova, E. L. Green, J. M. Law, D. I. Gorbunov, G. Chanda, S. Krämer, M. Horvatić, R. K. Kremer, J. Wosnitzer, and G. L. J. A. Rikken, *Phys. Rev. Lett.* **118**, 247201 (2017).
- [27] A. N. Vasil'ev, L. A. Ponomarenko, A. I. Smirnov, E. V. Antipov, Yu. A. Velikodny, M. Isobe, and Y. Ueda, *Phys. Rev. B* **60**, 3021 (1999).
- [28] J. Kikuchi, K. Ishiguchi, K. Motoya, M. Itoh, K. Inari, N. Eguchi, and J. Akimitsu, *J. Phys. Soc. Jpn.* **69**, 2660 (2000).
- [29] A. V. Prokofiev, R. K. Kremer, and W. Assmus, *J. Cryst. Growth* **231**, 498 (2001).
- [30] Y. Sakurai, H. Ohtsuka, and J.-i. Yamaki, *J. Electrochem. Soc.* **135**, 32 (1988).
- [31] Hua Ma, Shaoyan Zhang, Weiqiang Ji, Zhanliang Tao, and J. Chen, *J. Am. Chem. Soc.* **130**, 5361 (2008).
- [32] F. Cheng and J. Chen, *J. Mater. Chem.* **21**, 9841 (2011).
- [33] M. Ghiyasiyan-Arani, M. Masjedi-Arani, and M. Salavati-Niasari, *J. Mater. Sci.: Mater. Electron.* **27**, 4871 (2016).
- [34] C. Calvo and D. Manolescu, *Acta. Cryst. B* **29**, 1743 (1973). Please note that we use a different setting ($P-1$) of space group No. 2) with the unit cell halved compared to that given by Calvo and Manolescu.
- [35] See Supplemental Material at <http://link.aps.org/supplemental/10.1103/PhysRevB.102.014436> for structure details including the temperature dependence of the lattice parameters, details of the DFT calculations, EPR results, and the Padé approximant of the QMC calculations.
- [36] H.-J. Koo and M.-H. Whangbo, *J. Solid State Chem* **156**, 110 (2001).
- [37] M.-H. Whangbo, D. Dai, and H.-J. Koo, *Dalton Trans.* **2004**, 3019 (2004).
- [38] J. Deisenhofer, R. M. Eremina, A. Pimenov, T. Gavrilova, H. Berger, M. Johnsson, P. Lemmens, H.-A. Krug von Nidda, A. Loidl, K.-S. Lee, and M.-H. Whangbo, *Phys. Rev. B* **74**, 174421 (2006).
- [39] H.-J. Koo and M.-H. Whangbo, *Solid State Sci.* **9**, 824 (2007).
- [40] Above $\sim 640^\circ\text{C}$, α -CuV₂O₆ peritectically decomposes to CuO and V₂O₅, see the detailed discussion in Ref. [29]. Before decomposition the triclinic structure transforms into a monoclinic structure with space group $C2/m$ (No. 12) [41].
- [41] A. M. Golubev, Ph.D. thesis, Technical University Stuttgart, 2020.
- [42] J. Rodríguez-Carvajal, *Physica B* **192**, 55 (1993).
- [43] Note that to fit their magnetic susceptibilities Vasil'ev *et al.* [27] and Kikuchi *et al.* [28] used the Bonner-Fisher results which were obtained assuming the exchange Hamiltonian, $\mathcal{H} = 2J \sum_i \vec{S}_i \vec{S}_{i+1}$.
- [44] A. Abragam and B. Bleaney, *Electron Paramagnetic Resonance of Transition Ions* (Oxford University Press, New York, 1970).
- [45] M. E. Fisher, *Philos. Mag.* **7**, 1731 (1962).
- [46] J. C. LeGuillou and J. Zinn-Justin, *Phys. Rev. Lett.* **39**, 95 (1977).
- [47] J. Rodríguez-Carvajal, BASIREPS: A program for calculating irreducible representations of space groups and basis functions for axial and polar vector properties. Part of the FULLPROF suite of programs available at <http://www.ill.eu/sites/fullprof/>
- [48] C. Ritter, *Solid State Phenom.* **170**, 263 (2011).
- [49] D. C. Johnston, R. K. Kremer, M. Troyer, X. Wang, A. Klümper, S. L. Bud'ko, A. F. Panchula, and P. C. Canfield, *Phys. Rev. B* **61**, 9558 (2000).
- [50] R. L. Carlin, *Magnetochemistry* (Springer Verlag, Berlin, 1986).